

The symmetry problem of the *Fermi* and eROSITA bubbles: A proof-of-concept study

PO-HSUN TSENG ¹, H.-Y. KAREN YANG ^{2, 3, 4}, HSI-YU SCHIVE ^{1, 5, 6, 4}, CHUN-YEN CHEN,⁷ AND TZIHONG CHIUH ^{1, 5, 6}

¹*Institute of Astrophysics, National Taiwan University, Taipei 10617, Taiwan*

²*Institute of Astronomy, National Tsing Hua University, Hsinchu 30013, Taiwan*

³*Center for Informatics and Computation in Astronomy, National Tsing Hua University, Hsinchu 30013, Taiwan*

⁴*Physics Division, National Center for Theoretical Sciences, Taipei 10617, Taiwan*

⁵*Department of Physics, National Taiwan University, Taipei 10617, Taiwan*

⁶*Center for Theoretical Physics, National Taiwan University, Taipei 10617, Taiwan*

⁷*Institute of physics, National Taiwan University, Taipei 10617, Taiwan*

ABSTRACT

Keywords: *Fermi* bubbles, eROSITA bubbles, cosmic rays

1. INTRODUCTION

The detection of the *Fermi* bubbles (Su & Finkbeiner 2012; Ackermann et al. 2014; Narayanan & Slatyer 2017), two large bubbles symmetrically extending about 50 degrees above and below the Galactic plane, is one of the great discoveries made with *Fermi* Large Area Telescope (Atwood et al. 2009).

The gamma-ray emission of the *Fermi* bubbles is observed in the energy range of $1 \lesssim E_\gamma \lesssim 100$ GeV and has an almost spatially uniform hard spectrum, sharp edges and an approximately flat brightness distribution.

Over the course of a decade, the first all-sky X-ray survey with high-spatial resolution (Predehl et al. 2021) from eROSITA (Predehl et al. 2020) also reveals a giant hourglass-shaped structure (eROSITA bubbles hereafter) at the GC, extending about twice as large as the *Fermi* bubbles. The large-scale X-ray structure shows that the intrinsic size of the bubbles is 14 kiloparsecs across (Predehl et al. 2021), and displays morphological symmetry about the Galactic plane as the *Fermi* bubbles.

Their symmetry about the GC suggests that they originate from powerful energy injections from the GC, possibly related to nuclear star formation (Crocker & Aharonian 2011; Carretti et al. 2013) or past active galactic nucleus (AGN) activity (Guo & Mathews 2012; Yang & Ruszkowski 2017).

Early attempts (Sarkar et al. 2015; Yang & Ruszkowski 2017; Zhang & Guo 2020) to model the symmetric *Fermi* and eROSITA bubbles (collectively we call the Galactic bubbles) assumed that the jet is vertical to the Galactic plane. However, observation (Gallimore et al. 2006) has proposed that there is a lack of preferred orientation of jets with respect to the rotation axis of a galactic plane (disc normal, hereafter). In contrast, a number of galaxies in which the jets are oblique to the disc normal (e.g. NGC 3079, Cecil et al. 2001; NGC 1052, Dopita et al. 2015), including galaxies in which the jets lie in the plane of the disc (e.g. IC 5063, Morganti et al. 2015).

To this end, this work introduces a dense thin disc of interstellar medium around a jet source to deflects and decelerates the inclined jets, in an attempt to resolve the symmetry problem of the Galactic bubbles.

The main purpose of this study is to use three-dimensional special relativistic hydrodynamics simulations involving CR jet injections from the central SMBH in the Galaxy to investigate whether the *inclined* jet scenario is able to produce the *symmetric* Galactic bubbles that are consistent with the observed features, including the shape, the surface brightness, and the spectra of *Fermi* bubbles (Ackermann et al. 2014) and microwave haze (Dobler & Finkbeiner 2008; Ade et al. 2013).

This paper is organized as follows. In Section 2, we describe the numerical techniques and initial conditions employed. We directly compare the morphology of the Galactic bubbles with observation, and also show the simulated gamma-ray and microwave spectra compared

with observations in Section 3. Finally, we summarize our findings in Section 4.

2. METHODOLOGY

We used the GPU-accelerated special relativistic hydrodynamics AMR code (GAMER-SR) developed at the National Taiwan University (Schive et al. 2010, 2018; Tseng et al. 2021) to carry out the simulations of the Galactic bubbles by CR and relativistic fluid injections from the GC.

The CRs are advected with the thermal gas, and in return the velocities of gas can react to the gradients of the CR pressure via the source term containing spatial divergence of fluid velocities.

Although the high-energy CRe (10 – 100 GeV) plays a crucial role in reproducing the γ -ray map within the range of 1 – 100 GeV, we assume the pressure of CRe is much less than that of gas throughout the simulation so that we, and the *Fermi* bubbles can be outlined against the eROSITA bubbles.

As stressed by Yang et al. (2012), CR diffusion has an insignificant effect on the overall morphology of the *Fermi* bubbles, but only sharpens the edges of the simulated bubbles by the interplay between anisotropic CR diffusion and magnetic fields with suppressed perpendicular diffusion across the bubble surface. Moreover, the bubbles should be weak due to adiabatic expansion, and thus the magnetic fields has a little effect on the overall dynamics. For these two reasons, we have ignored the CR diffusion and the magnetic field throughout the simulation.

We do not simulate the spectral evolution of the CR, and we neglected the cooling and heating processes of CRs, such as energy losses due to synchrotron and inverse Compton emission, and reacceleration in shocks/turbulences.

In this approach, we treat CRs as a single species without distinction between electrons and protons, that cannot react to the gas via the application of CRe pressure, and solve directly for the evolution of CR energy density e_{cr} as a function of \mathbf{r} and t .

Since the relativistic fluid ejected by the jet source is quickly stalled off and slowed down by a dense ISM disc in a short time, and the relativistic fluid accounts for a little minority of total mass inside the simulation box, we still use the Newtonian gravity to attack this problem.

The governing equations solving the special relativistic ideal fluid including CR advection, and dynamical coupling between the thermal gas and CRs without CR diffusion can be written a succinct form as

$$\partial_t D + \partial_j (D U^j / \gamma) = 0, \quad (1a)$$

$$\partial_t M^i + \partial_j (M^i U^j / \gamma + p_{\text{gas}} \delta^{ij}) = -\rho \partial_i \Phi, \quad (1b)$$

$$\partial_t \tilde{E} + \partial_j [(\tilde{E} + p_{\text{gas}}) U^j / \gamma] = 0, \quad (1c)$$

$$\partial_t (\gamma e_{\text{cr}}) + \partial_j (e_{\text{cr}} U^j) = -p_{\text{cr}} \partial_j U^j, \quad (1d)$$

where the five conserved quantities of gas D , M^i , and \tilde{E} are the mass density, the momentum densities, and the reduced energy density, respectively. The reduced energy density is defined by subtracting the rest mass energy density of gas from the total energy density of gas. γ and U^j are the temporal and spatial component of four-velocity of gas. ρ is the gas density in the local rest frame defined by D/γ . p_{gas} is the gas pressure. p_{cr} and e_{cr} are the CR pressure and CR energy density measured in the local rest frame. Φ is the gravitation potential. c is the speed of light, and δ^{ij} is the Kronecker delta notation. Throughout this paper, Latin indices run from 1 to 3, except when stated otherwise.

The set of Equation (1) is closed by using the Taub-Mathews equation of state (Taub 1948; Mathews 1971) that approximates the exact EoS (Synge 1957) for ultra-relativistically hot gases coexisting with non-relativistically cold gases.

GAMER-SR adopts a new algorithm (Tseng et al. 2021) to convert between primitive (ρ , U^j , p) and conserved variables (D , M^j , \tilde{E}), significantly reducing numerical error caused by catastrophic cancellations that commonly occur within the regions with high Mach number flows. e.g., jet-ISM interaction zones.

GAMER-SR also adaptively and locally reduce the min-mod coefficient (Tseng et al. 2021) within the failed patch group. Doing so provides an elegant way to avoid the use of pressure/density floor, being unnatural but widely used in almost publicly available codes.

2.1. The Galactic and Disk Models

As a proof-of-concept study, we approximate conventionally axisymmetric stellar potential of Milky Way by a plane-parallel potential that is symmetric about the mid-plane $z = 0$ in a simulation box size of $14 \times 14 \times 28$ kpc, slightly larger than the size of eROISTA bubbles.

The plane-parallel potential is fixed throughout our simulations and given by

$$\Phi_{\text{total}}(z) = \Phi_{\text{bulge}}(z) + \Phi_{\text{halo}}(z), \quad (2)$$

where

$$\Phi_{\text{bulge}}(z) = 2\sigma_{\text{bulge}}^2 \ln \cosh \left(z \sqrt{\frac{2\pi G \rho_{\text{bulge}}^{\text{peak}}}{\sigma_{\text{bulge}}^2}} \right) \quad (3)$$



Figure 1. The density profile of the isothermal disc (red pluses) and atmosphere (blue crosses) along the positive z -axis. The density distribution is derived from hydrostatic equilibrium, the interface ($z = 0.1$) between the isothermal disc and the atmosphere is pressure balanced.

is the potential of an isothermal slab mainly contributed by stars around the Galactic bulge, and $\Phi_{\text{halo}}(z) = v_{\text{halo}}^2 \ln(z^2 + d_h^2)$ is a plane-parallel dark logarithmic halo potential.

With the recourse to the isothermal and hydrostatic equilibrium conditions, and assuming the interfaces between isothermal disc and atmosphere are in thermal pressure equilibrium, we can write the steady-state gaseous density distributions, confined in the total potential, of the disc and the Galactic atmosphere as

$$\rho_{\text{isoDisk}}(z) = \rho_{\text{isoDisk}}^{\text{peak}} \exp \left[-\frac{\Phi_{\text{total}}(z)}{k_B T_{\text{isoDisk}}/m_p} \right] \quad (4a)$$

, if $|z| < z_0$

$$\rho_{\text{atmp}}(z) = \rho_{\text{atmp}}^{\text{peak}} \exp \left[-\frac{\Phi_{\text{total}}(z)}{k_B T_{\text{atmp}}/m_p} \right] \quad (4b)$$

, otherwise,

where m_p is the proton mass, T_{isoDisk} and T_{atmp} is the temperature of the isothermal disc and atmosphere, $\rho_{\text{isoDisk}}^{\text{peak}}$ and $\rho_{\text{atmp}}^{\text{peak}}$ is the peak mass density of the disc and atmosphere on the mid-plane $z = 0$.

We tabulate parameters in the first four categories of Table 1, except for $\rho_{\text{atmp}}^{\text{peak}}$ that can be derived from the other known parameters and thermal pressure equilibrium condition on the interfaces ($z = \pm z_0$) between the disc and atmosphere.

The density profile of Equation (4) is shown in Figure 1. Beyond the core radius (~ 2 kpc) the gaseous density decreases rapidly as a power-law.

To quantify the synchrotron radiation as a function of position, it is essential to start the simulation with a more realistic magnetic field distribution. To this end, for our fixed magnetic field we adopt the default exponential model in GALPROP (Strong et al. 2007) which has the following spatial dependence:

$$|\mathbf{B}(R, z)| = B_0 \exp \left[-\frac{z}{z_0} \right] \exp \left[-\frac{R}{R_0} \right], \quad (5)$$

where $R = \sqrt{x^2 + y^2}$, B_0 is the average field strength at the GC and z_0 and R_0 are the characteristic scales in the vertical and radial directions, respectively. We adopt $z_0 = 2$ kpc and $R_0 = 10$ kpc, which are best-fitting values in the GALPROP model to reproduce the observed large-scale 408 MHz synchrotron radiation in the Galaxy. We choose $B_0 = 50 \mu\text{G}$ based on the observed field strength at the GC (Crocker et al. 2010).

2.2. The Clumpy Multiphase Interstellar Medium

A crucial component in our work is the clumpy ISM disc initialized by the publicly available pyFC code ¹.

pyFC randomly generates dimensionless 3D scalar field $f(\mathbf{x})$ that obeys the log-normal probability distribution with mean μ and dispersion σ , and follows the power-law Kolmogorov spectrum

$$D(\mathbf{k}) = \int k^2 \hat{f}(\mathbf{k}) \hat{f}^*(\mathbf{k}) d\Omega \propto k^{-\beta}, \quad (6)$$

where $\hat{f}(\mathbf{k})$ is the Fourier transform of $f(\mathbf{x})$. The spectrum $D(\mathbf{k})$ in the Fourier space is characterized by the power-law index $\beta = 5/3$, the Nyquist limit k_{max} , and the lower cutoff wave number k_{min} . k_{max} is one-half of the spatial resolution within disc, and k_{min} is 375.0, corresponding to the maximum size of an individual clump ~ 20 pc. Lewis & Austin (2002) and Wagner et al. (2012) have outlined a detailed procedure for constructing a clumpy scalar field, and we do not repeat here.

The density of clumpy disc can thus be obtained by taking the scalar products of $f(\mathbf{x})$ with $\rho_{\text{isoDisk}}(z)$ over all cells within the disc, i.e., $\rho_{\text{ismDisk}}(\mathbf{x}) = f(\mathbf{x}) \rho_{\text{isoDisk}}(z)$. Also, the thermal pressure equilibrium within the clumpy disc implies that the temperature of disc is $T_{\text{ismDisk}}(\mathbf{x}) = T_{\text{isoDisk}}(z) \rho_{\text{isoDisk}}(z) / \rho_{\text{ismDisk}}(\mathbf{x})$.

Table 1 summarize the parameters of the clumpy disc and their references.

On the basis of this setup, we cover the AMR base level with $16 \times 16 \times 32$ root cells, refined progressively on the mid-plane $z = 0$ based on the gradient of mass

¹ <https://pypi.python.org/pypi/pyFC>



Figure 2. The volume filling factor as a function of initial number density within the disc without jet source. The vertical bands from left to right depict the allowable number densities (Ferrière 2001) for hot ionized, warm neutral (WNM), warm ionized (WIM), cold neutral mediums (CNM), and molecular clouds.

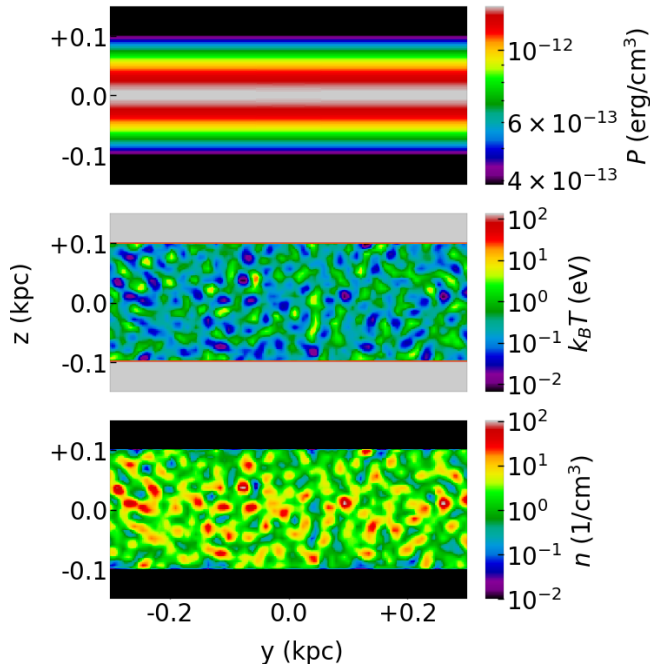


Figure 3. Close-up view of the initial pressure (top), temperature (middle), and number density (bottom) slices in the y-z plane through the center of the disc.

density. We also restrict the refinement level at 7 within the cold disc so that a molecular cloud can be adequately resolved by approximately 30 cells along their diameter, 20 pc.

Figure 2 plots the volume filling factor as a function of initial number density within the disc without jet source.

Figure 3 shows a close-up view of the pressure, temperature, and number density slices in the y-z plane through the center of the disc.

2.3. Inclined jet injection

Motivated by these observations, we simulate the jet with an inclination angle 45° with respect to the Galactic plane in order to release the caveat that the jet direction must be perpendicular to the Galactic plane, and in particular to investigate the effect of the jet-disc misalignment on the symmetry of bubbles.

A few additional quantities are used to characterize the jets: the density contrast between the thermal gas contained in the jet source and the ambient gas, $\rho_{\text{jet}}/\rho_{\text{amb}} = 10^{-3}$, the temperature contrast, $T_{\text{jet}}/T_{\text{amb}} = 2 \times 10^4$, the pressure ratio of CR to gas is 0.18, and the flow 4-velocity inside the jet source $\beta\gamma = 0.6$ along the symmetric axis of cylinder. The jet power is thus 3.2×10^{42} erg/s, resulting in the Eddington ratio 0.008.

Note that as we inject the jets at the center of the clumpy disc, we define the ambient gas density by the peak density of the isothermal disc on the mid-plane $z = 0$ (i.e. $\rho_{\text{isoDisk}}^{\text{peak}}$), as opposed to the *clumpy* density around the jet source, to avoid ambiguous definition.

The bipolar jets are constantly ejected from a cylindrical source at the beginning of simulation ($t = 0$) and suddenly quenched at $t = 1.2$ Myr before fully breaking out the disc. Without quenching, the Galactic bubbles at the present time will be asymmetric about the Galactic plane. The jet duration (1.2 Myr) allows the total ejected energy to be 1.2×10^{56} erg, bracketed by 8×10^{55} and 1.3×10^{56} erg, estimated by Predehl et al. (2020).

The diameter and height of cylindrical source are 4 pc, leading to the source volume $\sim 50 \text{ pc}^3$ is much smaller than that of an individual clump by a factor of about 83. By intentionally reducing the volume ratio of the jet source to an individual clump, we can mitigate the effect of the randomness of the clumps on the bubbles. Moreover, we resolve the jet source with the highest refinement level 11, bringing the finest spatial resolution up to 0.4 pc.

3. RESULTS

3.1. Morphology and properties of Galactic bubbles

Figure 4 shows the slices of pressure (top), temperature (middle), number density (bottom) at the end of simulation $t = 12.39$ Myr. The slices pass through the bipolar jet source injecting along $z = -y$ direction.

The fiducial run (leftmost column) with the initial condition specified in Section 2 shows that the edge of the outermost bubbles is indeed a forward shock, expanding 12.5 kpc above and below the Galactic plane, and with a radius of about 6.8 kpc along the plane. We note that the overall extent of the outermost bubbles is comparable to the two spherical objects of a radius 6-7

Parameter	Description	Value	Reference
Static stellar potential			
σ_{bulge}	Velocity dispersion of bulge	100 km·s ⁻¹	(Valenti et al. 2018)
$\rho_{\text{bulge}}^{\text{peak}}$	Peak average density of bulge	4×10^{-24} g·cm ⁻³	N/A
Static dark halo potential			
v_{halo}		131.5 km·s ⁻¹	(Johnston et al. 1995)
d_{h}	Core radius	12 kpc	"
Atmosphere			
T_{atmp}	Temperature of atmosphere	10 ⁶ K	(Tepper-García et al. 2015)
Isothermal disc			
z_0	Scale height of disc	100 pc	(Ferrière 2001)
T_{isoDisk}	Temperature of disc	10 ³ K	"
$\rho_{\text{isoDisk}}^{\text{peak}}$	Peak mass density of disc	10^{-23} g·cm ⁻³	"
Clumpy disc			
$\dagger k_{\text{min}}$	Cutoff wave number	375.0	(Ferrière 2001)
μ	Mean of scalar field	1.0	N/A
$\ddagger \sigma$	Dispersion of scalar field	5.0	(Federrath et al. 2010)
β	Power law index	-5/3	N/A

$\dagger k_{\text{min}} = 375.0$ leads to the size of an individual molecular cloud ~ 100 pc.

\ddagger In numerical simulations of turbulence, Federrath et al. (2010) find $\sigma \sim 3.6$ and 35 for solenoidal (divergence-free) and compressive (curl-free) driving force, respectively, so that our adopted value of 5 is closer to their solenoidal result.

Table 1. Parameters of the disc, atmosphere, and gravitational potential in the simulation.

kpc proposed by Predehl et al. (2020) for modeling the eROSITA bubbles.

The left column of Figure 5 shows the profiles cut at the positive z-axis in Figure 4. The temperature profile in the left column indicates that most of the region between the forward shock and the turbulent region is around 0.3-0.4 keV (Miller & Bregman 2016; Kataoka et al. 2018).

Followed by the forward shock is a turbulent and high temperature (~ 2 keV) plasma. By observing X-ray absorption lines through the hot gaseous halo along many different sight lines in the sky, Miller & Bregman (2012) found that the ratio between O viii and O vii column densities is enhanced for sight lines that pass through the Fermi bubbles, indicating gas temperature of a few times keV inside the bubbles.

Comparison between the clumpy (first column from left) and the smooth disc (second) in a stratified atmosphere shows that the initial density distribution of the dense disc has an insignificant effect on the overall dynamics of bubbles. However, the outermost bubbles arising from the smooth disc in an uniform atmosphere (third) is spherical-shape, suggesting the stratification facilitates the outermost bubbles elongation significantly. Also, the two rightmost columns reveal that the development of the innermost bubbles (dashed box) is always associated with the disc, and without the disc, the outermost bubbles and the

turbulent region will be oblique, indicating the dense disc is crucial for the symmetry of the Galactic bubbles and for the innermost bubbles formation.

3.2. X-ray

The X-ray emissivity is computed for each computational volume cell using the MEKAL model (Mewe et al. 1985; Kaastra & Mewe 1993; Liedahl et al. 1995) implemented in the utility XSPEC (Arnaud 1996), assuming solar metallicity. The X-ray intensity map are then generated by projecting the emissivities along lines of sight pointing away from the solar position at $(R_{\odot}, 0, 0) = (8, 0, 0)$ kpc with angular resolutions of 0.5 degrees

We point out that the projections throughout this paper is ‘perspective’, which has the effect of making distant object appear smaller than the same object in the near distance, in order to facilitate a reliable interpretation of simulated all-sky map, and also that the observed X-ray emission is contributed by all the gas in the Milky Way halo, which likely extends to a radius of ~ 250 kpc (Blitz & Robishaw 2000; Grcevich & Putman 2009), much bigger than our simulation box. Therefore, we first compute the X-ray emissivity from the simulated gas within a radius of 25 kpc away from the GC. Then, beyond 25 kpc the gas is assumed to be isothermal with $T = 10^6$ K and follows out to a radius of

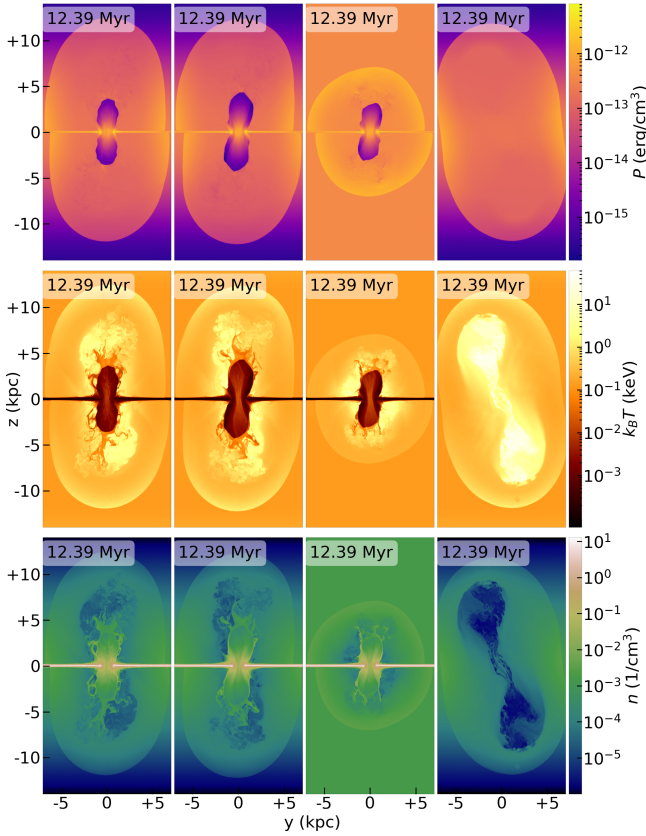


Figure 4. The slices of pressure (top), temperature (middle), and number density (bottom) at the end of simulation $t = 12.39$ Myr. The slices pass through a bipolar jet source injecting along $z = -y$ direction for a duration $t = 0$ – 1.2 Myr. Comparison between the clumpy (first column from left) and the smooth disc (second) in a stratified atmosphere shows that the initial density distribution of the dense disc has an insignificant effect on the overall dynamics of bubbles. However, the outermost bubbles arising from the smooth disc in an uniform atmosphere (third) is spherical-shape, suggesting the stratification facilitates the outermost bubbles elongation significantly. Also, the two rightmost columns reveal that the development of the innermost bubbles (dashed box) is always associated with the disc, and without the disc, the outermost bubbles and the turbulent region will be oblique, indicating the dense disc is crucial for the symmetry of the Galactic bubbles and for the innermost bubbles formation.

250 kpc the observed density profile of (Tepper-García et al. 2015).

Figure 6(a) shows the comparison between simulated (top) and observed (bottom) all-sky map in the range 0.6 – 1.0 keV at the present time. In the simulated map, the red arrow at the center of map represents the direction of the bipolar jet, constantly ejecting at an angle of 45° to the disc normal in 1.2 Myr.

Figure 6(b) displays the simulated count rate profiles (red) in the same energy band as Figure 6(a) cut at



Figure 5. The profile along the positive z -axis in Figure 4.

various galactic latitudes (as labelled), compared with the observation (black). Figure 6 is quite revealing in several ways.

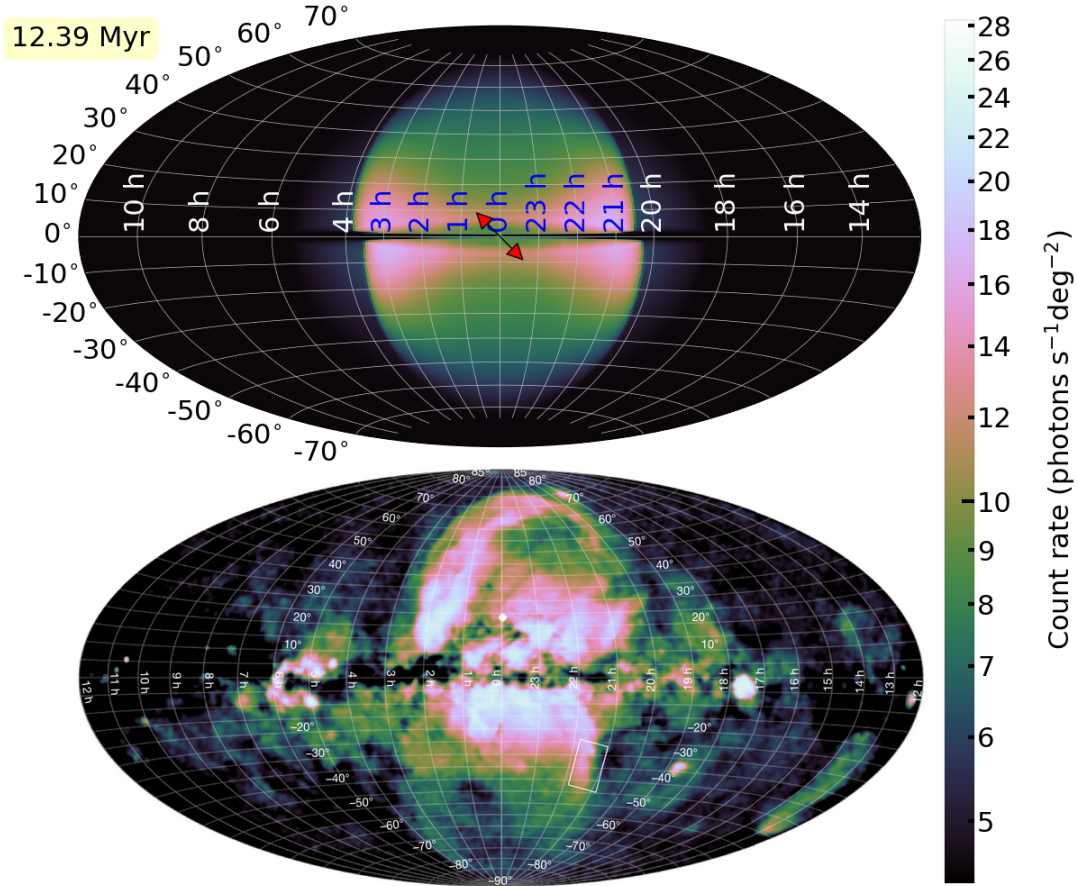
First, the broad agreement between simulated and observed X-ray maps hints that the full vertical extent of the eROSITA bubbles can be properly formed by an inclined jet within a thin disk of dense interstellar medium.

Second, as shown in Figure 4, the half-width of the outermost bubbles is around 7 kpc, corresponding to an half angular width $\sin^{-1}(7 \text{ kpc}/R_\odot) \sim 122^\circ$, which is as wide as the eROSITA bubbles in the simulated X-ray map (top panel in Figure 6(a)). We therefore suggest that the nature of eROSITA bubbles is indeed a forward shocks that have been driven into the northern and the southern Galactic halo, as previously proposed by Predehl et al. (2020).

Third, the innermost bubbles shown in Figure 4, even though with high column density, is invisible in the simulated X-ray map as the temperature of innermost bubbles is around 1 – 10 eV (see the temperature slice in Figure 4). Consequently, the X-ray emission within the innermost bubbles is severely suppressed by the cutoff $\exp[-h\nu/k_B T]$ in the thermal Bremsstrahlung emissivity. This is the reason why the innermost bubbles is unseen in the observation.

3.3. Gamma-ray and microwave spectra: constraint on the CRe spectral index

In this section, we give the constraint on the CRe spectral index by comparing the simulated gamma-ray and microwave spectra with the observed spectra of the Fermi bubbles Ackermann et al. (2014) and



(a) Simulated (top) and observed (bottom; [Predehl et al. 2020](#)) count rate (photons $\text{s}^{-1} \text{deg}^{-2}$) in the $0.6 - 1.0$ keV range. Throughout this paper we show sky maps in Galactic coordinates centered on the Galactic center using a Hammer-Aitoff projection, and observed from the solar system. The red arrow at the center of the top panel depicts the direction of the bipolar jet, constantly ejecting at an angle of 45° to the disc normal in 1.2 Myr.



(b) Comparison of simulated (red) and observed (black; [Predehl et al. 2020](#)) one-dimensional count rate profiles in the same energy band as Figure 6(a), cut at various Galactic latitudes (as labelled).

Figure 6.

the microwave haze (Dobler & Finkbeiner 2008), respectively.

The simulated gamma-ray and microwave spectra is based on the IC scattering and synchrotron from CRe, in which the CRe spectrum follows a power-law distribution ranging from $m_e c^2$ (0.5 MeV) to $1.1 \times 10^6 m_e c^2$ (562.1 GeV), where $m_e c^2$ is the rest mass energy of an electron.

The IC emissivity of the upscattered photons at the energy ϵ_1 is computed for each computational cell in our simulations using the Klein-Nishina IC cross-section (Jones 1968; Blumenthal & Gould 1970) to handle the scattering between ultra-relativistic CRe and photons in the ISRF:

$$\frac{dE}{dt d\epsilon_1 dV} = \frac{3}{4} \sigma_T c \mathbb{C} \epsilon_1 \int_{\epsilon_{\min}}^{\epsilon_{\max}} \frac{n(\epsilon)}{\epsilon} d\epsilon \int_{\gamma_{\min}(\epsilon)}^{\gamma_{\max}} \gamma^{-(p+2)} f(q, \Gamma) d\gamma, \quad (7a)$$

$$f(q, \Gamma) = 2q \ln q + (1 + 2q)(1 - q) + 0.5(1 - q) \frac{(\Gamma q)^2}{1 + \Gamma q}, \quad (7b)$$

$$q = \frac{\epsilon_1 / \gamma m_e c^2}{\Gamma (1 - \epsilon_1 / \gamma m_e c^2)}, \quad (7c)$$

$$\Gamma = \frac{4\epsilon\gamma}{m_e c^2}, \quad (7d)$$

$$\gamma_{\min}(\epsilon) = 0.5 \left(\frac{\epsilon_1}{m_e c^2} + \sqrt{\left(\frac{\epsilon_1}{m_e c^2} \right)^2 + \frac{\epsilon_1}{\epsilon}} \right), \quad (7e)$$

where σ_T is the Thomson cross section, c speed of light, $n(\epsilon)$ the energy distribution of the photon number density in ISRF given by Porter et al. (2017), γ the Lorentz factor of CRe, \mathbb{C} and p are the normalization constant and spectral index of CRe power-law spectrum. $\gamma_{\min}(\epsilon)$ is the minimum Lorentz factor of CRe that allows incident photons to scatter from energy ϵ to ϵ_1 . γ_{\max} is the maximum CRe Lorentz factor in the spectrum.

We perform the double integration in Equation (7) on each cell over the range of CRe Lorentz factor, and the range of incident photon energy between $\epsilon_{\min} = 1.13 \times 10^{-4}$ eV (cosmic microwave background radiation) and $\epsilon_{\max} = 13.59$ eV (optical starlight) to obtain the simulated IC emissivities.

The synchrotron emissivity with an isotropic electron pitch angle distribution is given by Blumenthal & Gould (1970):

$$\frac{dE}{dt d\nu dV} = \frac{4\pi \mathbb{C} e^3 B^{0.5(p+1)}}{m_e c^2} \left(\frac{3e}{4\pi m_e c} \right)^{0.5(p-1)} a(p) \nu^{-0.5(p-1)}, \quad (8a)$$

$$a(p) = \frac{2^{0.5(p-1)} \sqrt{3} \Gamma[(3p-1)/12] \Gamma[(3p+9)/12] \Gamma[(p+5)/4]}{8 \sqrt{\pi} (p+1) \Gamma[(p+7)/4]}, \quad (8b)$$

where Γ is gamma function, B is the magnetic field strength defined in Equation (5).

For a given longitude and latitude range, the simulated spectra are computed by projecting emissivities as we project X-ray emissivities in Section 3.2, and then we average the spectra over all the sight lines within the region on sky.

Figure 7 shows the simulated microwave (left) and gamma-ray (right) spectra averaged over the different patches (shown in the legends) of the sky. The row from top to bottom shows the microwave (left) and gamma-ray (right) spectra with CRe spectral index 2.2, 2.4 and 2.6, respectively. Several points are worth specific comment.

First, we find that the simulated gamma-ray spectra are well fitted by the CRe spectral index 2.4 (the middle row), despite the simulated microwave spectra are marginally consistent with the observed.

Second, the simulated and observed gamma-ray spectra is nearly latitude independent, and characterized by a broad bump that roughly peaks around ~ 10 GeV. However, the high-latitude spectrum tends to be slightly dimmer than low-latitude probably because the optical intensity in ISRF decays with increasing latitude.

Third, the gamma-ray spectra for all latitudes indicate a spectral cutoff around energies 400 – 500 GeV, consistent with the observed cutoff energy. This is expected since the upscattered high-energy photons ($\epsilon_1 \sim 450$ GeV) mainly arise from the scatterings between the relativistic CRe ($\gtrsim 408$ GeV) and optical starlight ($\epsilon \sim 10$ eV), and therefore Equation (7e) can be reduced to $\epsilon_1 \sim \gamma m_e c^2$ in the Klein-Nishina limit (i.e. $\epsilon_1 \epsilon \gg (m_e c^2)^2$), implying most of the CRe energy is carried away by the upscattered photons.

Fourth, the good agreement between the simulated and observed gamma-ray/microwave spectra imply that the emission of the Fermi bubbles and the microwave haze can be produced by the same high-energy electrons via inverse Compton scatterings and synchrotron radiations in the presence of ISRF and

magnetic fields, respectively, as previously suggested (Su et al. 2010; Dobler 2012).

Finally, we display the morphology of the *Fermi* bubbles that emit gamma-rays from the inverse Compton scattering of ISRF by CRe with the best-fit CRe spectral index 2.4

We close on a speculative note that predicts an existence of a third bubbles for future observations.

Figure 8 shows the simulated gamma-ray photon flux compared with the observed one in the energy bin 76.8 – 153.6 GeV. One can see that the symmetric of the *Fermi* bubbles can also be realized by oblique jets as the eROSITA bubbles.

4. CONCLUSIONS

In this work, we introduce a thin, dense disk composed of interstellar medium to divert the inclined jet at an angle 45° to the disk normal in the past energetic event of the central SMBH.

Also, We investigate the properties of the Galactic bubbles and the microwave haze using 3D special relativistic hydrodynamic simulations of CR injection from the SMBH assuming the leptonic model.

Our findings are as follows.

- The Galactic bubbles are nearly symmetric about the Galactic plane albeit the jet is at an angle 45° with respect to the disc normal. The broad agreement between simulated and observed multiwavelength features provides supporting evidence for the inclined jet scenario, and also releases the caveat given by earlier simulation-based studies: the jets shall be vertical to the disc normal.
- The randomness of clumpy disk has a insignificant impact on the overall dynamic of the Galactic bubbles. The ambient stratification facilitates the eROSITA bubbles elongation significantly. The development of the inverse shocks are always associated with the dense disc.
- The edge of the eROSITA bubbles is a forward shock, originally driven by an oblique bipolar jets emanating from the GC 12.39 million years ago, and significantly stretched by the stratified atmosphere afterwards.
- Followed by the forward shock is a contact discontinuity, which we interpret as the edge of the *Fermi* bubbles. The nature of the *Fermi* bubbles is essentially a turbulent and high-temperature (~ 1 keV) plasma in pressure balance with the external medium. Associated with the Galactic magnetic field will lead to the stochastic acceleration of CRe, and probably balanced with the IC and synchrotron cooling. We will investigate the competition between CRe acceleration and radiative cooling in a future work.
- According to the microwave and leptonic gamma-ray spectra, the best-fitting CRe power-law index is found to be -2.4.
- The same leptotonic CRe can simultaneously account for the *Fermi* bubbles and haze emission suggested that they are physically related around the GC, and that the magnetic fields within the bubbles are close to the exponentially distributed Galactic magnetic field.

We have found qualitative similarities between the results our simulations and the observed spectrum and morphological structure of the Galactic bubbles.

Since the jets encounter a larger column depth of clouds along their path, they interact more strongly with the dense ISM. The jets do not immediately clear a channel along the inclined axis of launch. Rather, the dense clouds deflect the jets, which then decelerate and launch a sub-relativistic outflow along the minor axis following the path of least resistance.

Assuming that a relativistic electron population of spectral index $x = 2.2$ gives rise to the microwave haze via synchrotron emission.

DATA AVAILABILITY

The data underlying this article are available in the article and in its online supplementary material.

REFERENCES

- Ackermann M., et al., 2014, *The Astrophysical Journal*, 793, 64
- Ade P. A. R., et al., 2013, *Astronomy & Astrophysics*, 554, A139
- Arnaud K. A., 1996, in Jacoby G. H., Barnes J., eds, *Astronomical Society of the Pacific Conference Series* Vol. 101, *Astronomical Data Analysis Software and Systems V*. p. 17



Figure 7. Simulated microwave spectra (colored lines in left) averaged over $20^\circ < |b| < 30^\circ$, $|l| < 10^\circ$. The data point represents the *WMAP* data in the 23 GHz K band and the shaded bow-tie area indicates the range of synchrotron spectral indices allowed for the *WMAP* haze (Dobler & Finkbeiner 2008). Simulated gamma-ray spectra (colored lines in right column) of the *Fermi* bubbles calculated for a longitude range of $|l| < 10^\circ$ for different latitude bins. The gray band represents the observational data of Ackermann et al. (2014). The row from top to bottom shows the microwave (left) and gamma-ray (right) spectra with CRe spectral index 2.2, 2.4 and 2.6, respectively. The CRe cutoff energy is $1.1 \times 10^6 m_e c^2$ in all cases.



Figure 8. The observed (left) and simulated (right) photon flux in the energy bin 76.8 – 153.6 GeV. Note that the left panel is the photon flux of the diffuse component reconstructed by the D3PO algorithm (Selig et al. 2015) that analyzes the photon data from the *Fermi* Large Area Telescope (Atwood et al. 2009) and removes the contribution from point-like component. The red arrow at the center of the right panel depicts the direction of the bipolar jet, constantly ejecting at an angle of 45° to the disc normal in 1.2 Myr.



Figure 9. The slice of CR... p_{CR} is much less than p_{gas} ...

- Atwood W. B., et al., 2009, *The Astrophysical Journal*, 697, 1071
- Blitz L., Robishaw T., 2000,] 10.1086/309457, 541, 675
- Blumenthal G. R., Gould R. J., 1970, *Reviews of Modern Physics*, 42, 237
- Carretti E., et al., 2013, *Nature*, 493, 66
- Cecil G., Bland-Hawthorn J., Veilleux S., Filippenko A. V., 2001, *The Astrophysical Journal*, 555, 338
- Crocker R. M., Aharonian F., 2011, *Phys. Rev. Lett.*, 106, 101102
- Crocker R. M., Jones D. I., Melia F., Ott J., Protheroe R. J., 2010, *Nature*, 463, 65
- Dobler G., 2012, *The Astrophysical Journal*, 750, 17
- Dobler G., Finkbeiner D. P., 2008, *The Astrophysical Journal*, 680, 1222
- Dopita M. A., et al., 2015, *The Astrophysical Journal Supplement Series*, 217, 12
- Federrath C., Roman-Duval J., Klessen R. S., Schmidt W., Low M.-M. M., 2010, *Astronomy and Astrophysics*, 512, A81
- Ferrière K. M., 2001, *Rev. Mod. Phys.*, 73, 1031
- Gallimore J. F., Axon D. J., O'Dea C. P., Baum S. A., Pedlar A., 2006, *The Astronomical Journal*, 132, 546
- Grcevich J., Putman M. E., 2009,] 10.1088/0004-637x/696/1/385, 696, 385
- Guo F., Mathews W. G., 2012, *The Astrophysical Journal*, 756, 181
- Johnston K. V., Spergel D. N., Hernquist L., 1995, *The Astrophysical Journal*, 451, 598
- Jones F. C., 1968, *Physical Review*, 167, 1159
- Kaastra J. S., Mewe R., 1993, *A&AS*, 97, 443
- Kataoka J., Sofue Y., Inoue Y., Akita M., Nakashima S., Totani T., 2018, *Galaxies*, 6, 27
- Lewis G. M., Austin P. H., 2002, 1th Conference on Atmospheric Radiation
- Liedahl D. A., Osterheld A. L., Goldstein W. H., 1995, *ApJL*, 438, L115
- Mathews W. G., 1971, *ApJ*, 165, 147
- Mewe R., Gronenschild E. H. B. M., van den Oord G. H. J., 1985, *A&AS*, 62, 197
- Miller M. J., Bregman J. N., 2016, *The Astrophysical Journal*, 829, 9
- Morganti R., Oosterloo T., Oonk J. B. R., Frieswijk W., Tadhunter C., 2015, *Astronomy & Astrophysics*, 580, A1
- Narayanan S. A., Slatyer T. R., 2017, *Monthly Notices of the Royal Astronomical Society*, 468, 3051
- Porter T. A., Jóhannesson G., Moskalenko I. V., 2017, *The Astrophysical Journal*, 846, 67
- Predehl P., et al., 2020, *Nature*, 588, 227
- Predehl P., et al., 2021, *Astronomy & Astrophysics*, 647, A1
- Sarkar K. C., Nath B. B., Sharma P., 2015, *Monthly Notices of the Royal Astronomical Society*, 453, 3828
- Schive H.-Y., Tsai Y.-C., Chiueh T., 2010, *The Astrophysical Journal Supplement Series*, 186, 457
- Schive H.-Y., ZuHone J. A., Goldbaum N. J., Turk M. J., Gaspari M., Cheng C.-Y., 2018, *Monthly Notices of the Royal Astronomical Society*, 481, 4815
- Selig M., Vacca V., Oppermann N., Enßlin T. A., 2015, *Astronomy & Astrophysics*, 581, A126
- Strong A. W., Moskalenko I. V., Ptuskin V. S., 2007, *Annual Review of Nuclear and Particle Science*, 57, 285
- Su M., Finkbeiner D. P., 2012, *The Astrophysical Journal*, 753, 61
- Su M., Slatyer T. R., Finkbeiner D. P., 2010, *The Astrophysical Journal*, 724, 1044
- Synge J. L., 1957, North-Holland Pub. Co.; Interscience Publishers
- Taub A. H., 1948, *Physical Review*, 74, 328
- Tepper-García T., Bland-Hawthorn J., Sutherland R. S., 2015, *The Astrophysical Journal*, 813, 94

- Tseng P.-H., Schive H.-Y., Chiueh T., 2021, [Monthly Notices of the Royal Astronomical Society](#), 504, 3298
- Valenti E., et al., 2018, [A&AS](#), 616, A83
- Wagner A. Y., Bicknell G. V., Umemura M., 2012, [The Astrophysical Journal](#), 757, 136
- Yang H.-Y. K., Ruszkowski M., 2017, [The Astrophysical Journal](#), 850, 2
- Yang H.-Y. K., Ruszkowski M., Ricker P. M., Zweibel E., Lee D., 2012, [The Astrophysical Journal](#), 761, 185
- Zhang R., Guo F., 2020, [The Astrophysical Journal](#), 894, 117